Electronic Supporting Information for

Strong and Tough Conductive PVA Hydrogels Based on the Synergy of Acetic Acid Induction and Salting-out for Flexible Solid-State Supercapacitor

Weifeng Zhong, *Yufang Song*, *Jiwei Chen*, *Shuai Yang*, *Lihao Gong*, *Dongjian Shi*, *Weifu Dong*, and *Hongji Zhang**

The Key Laboratory of Synthetic and Biological Colloids, Ministry of Education, School of Chemical and Material Engineering, Jiangnan University, Wuxi, Jiangsu 214122, China.

*Corresponding author: Prof. Hongji Zhang
E-mail: hongjizhang@jiangnan.edu.cn

This PDF file includes:
Characterizations and Fig. S1-S13

Characterizations

An Attenuated total reflectance Fourier transform infrared spectrometer (ATR-FTIR, Nicolet iS50, USA) was used to analyze the molecular chemical structure of the gel samples in the wavenumber range of 650 to 4000 cm^{-1} with a nominal resolution of 4 cm^{-1}. A scanning electron microscope (SEM, Hitachi S-4800, Japan) was used to observe the morphologies of the gel and carbon cloth samples. Before SEM observation, the gel samples were rapidly frozen to quench by liquid nitrogen and then freeze-dried to reveal their cross-sectional structure. The surface of the samples was sputter-coated with gold to create a conductive environment. Raman spectra of carbon cloth and CC/PANI electrode were recorded on Renishaw InVia Plus from 500 to 3500 cm^{-1} under the laser excitation of 785 nm. Rheological tests were conducted using a DHR-3 rheometer (TA Instruments, USA) at 25 °C. And the samples were put between the parallel plate (20 mm in diameter) with a frequency range from 0.1 to 100 rad s^{-1} at a fixed strain of 0.1%.

Mechanical measurement. All mechanical tests were performed on a universal double-column bench testing machine (5967X, ITW Company, USA) at room temperature. For the tensile experiment, the samples were cut into dumbbell-shaped pieces (gauge length: 15 mm; inner width: 4 mm; thickness: 1-2 mm) and stretched at a crosshead speed of 50 mm min^{-1}. The strain was estimated as the length change relative to the initial length, and the stress was computed by dividing the force with the initial cross-sectional area of the sample. Elastic modulus E was estimated from the linear region slope of the stress-strain curve, while toughness (KJ m^{-3}) was defined as the area

under the stress-strain curve until the sample cracked. For the successive loading-unloading tests, the sample was stretched to 500% and unloaded at 50 mm min^{-1} for 8 times. The dissipated energy was evaluated from the closed area of the hysteresis loop between the loading-unloading curve.

Water content measurement. The water content (WC) of the PVA hydrogel was measured by comparing their weights before and after drying. The weight of the sample before drying was represented by m_w, and the constant weight after being dried in a vacuum oven at 60 °C for 3 days was represented by m_d. The water content was calculated as follows:

$WC(\%) = [(m_w-m_d)/m_w] \times 100\%$.

Crystallinity measurement. The crystallinities of the gel samples were measured by a differential scanning calorimeter (DSC 204 F1, NETZSCH-Gerätebau GmbH, Germany). Before DSC measurements, the PVA gels were first excess chemical crosslinked by soaking in an aqueous solution composed of glutaraldehyde, hydrochloric acid, and deionized water (volume ratio = 20:1:50) for 2 h to fix the amorphous PVA polymer chains, minimizing the extra crystallization during the freeze-drying process.[1] Subsequently, the samples were immersed in a large amount of DI water for 12 h to get rid of the residual small molecules. In a typical DSC measurement, the freeze-dried sample was heated up from 50 to 250 °C at a scanning rate of 20 °C min^{-1} under a nitrogen flow of 30 ml min^{-1}. The broad peak from 60 to 180 °C and the narrow peak from 200 to 250 °C on the curve of heat flow respectively correspond to the evaporation of the residual water and the melting of the PVA crystalline domains. Calculate the integration of the endothermic enthalpy of two regions, expressed as *Hw* and *Hc*, respectively. Therefore, the crystallinity of the dry samples (X_{dry}) can be calculated using the following equation: $X_{dry} = (Hc \times Hw^0) / [Hc^0 \times (Hw^0 - Hw)]$. With the water content (WC) of the swollen-state sample, the crystallinity in the swollen sample can be estimated as:

$X_{swollen}=X_{dry}$ (1-WC).

Where Hc^0 = 138.6 J g^{-1} is the enthalpy of the fusion of 100 wt% crystalline PVA measured at equilibrium melting point, Tm^0,[2] and Hw^0 = 2260 J g^{-1} is the latent heat of water evaporation.[3]

X-ray scattering. The wide-angle x-ray scattering (WAXS) testing was performed on the Bruker D8 diffractometer (German Bruker AXS, Germany) using Cu Kα radiation (λ = 0.154 nm) with the 2θ range from 5 to 60° at a scanning rate of 4° min^{-1}. The average size of crystalline domains (D) can be approximately calculated by Scherrer's equation:[4] $D = k\lambda/(\beta\cos\theta)$, where k is a dimensionless shape factor and is set as 1 if approximating the shape of the crystalline domain as a sphere, λ is the wavelength of the X-ray diffraction, β is the full width at half maximum of the peak, and θ is half of the diffraction angle. The small-angle X-ray scattering (SAXS) measurements were carried out at Xeuss 3.0 HR SAXS/WAXS System (Xenocs, France) with an X-ray of λ = 0.154 nm. The sample-to-detector distance was set at 1800 mm, covering the efficient scattering (q) range of 0.001-0.145 $Å^{-1}$. To identify the location of the peak intensity, we correct the intensity by multiplying the scattering intensity (I) with the scattering vector (q) and plotting it as Iq^2 vs q. The average distance between adjacent crystalline domains (L) can be estimated from the critical scattering vector (q_{max}) corresponding to the peak intensity, following the Bragg expression ($L = 2\pi/q_{max}$).

Electrochemical measurement. All the electrochemical performances of the capacitor device were measured on the CHI 660E electrochemical workstation (Chenhua, Shanghai). Electrochemical impedance spectra (EIS) were tested at the frequency range from 0.01 to 100000 Hz. The bulk resistance of the gel electrolyte (R) was the intersection of the curve at the real part. The ionic conductivity (σ, mS cm^{-1}) was calculated as $\sigma = L / (R \times S)$, where L was the thickness of the gel

electrolyte and S was the cross-sectional area of the electrolyte. Cyclic voltammetry (CV) of the supercapacitor was carried out at the potentials of 0.8 V at scan rates of 20-200 mV s^{-1}. Galvanostatic charge-discharge (GCD) was performed at 0.8 V at different current densities of 0.5-3 mA cm^{-2}. The specific capacitance C_S (mF cm^{-2}) was calculated from the GCD curves by the equation: [5,6] $C_S = (I \times \Delta t) / (S \times \Delta V)$, where I is the charge-discharge current (mA), Δt is the discharge time (s), S is the surface area of the electrode (cm^2), and ΔV is the potential window (V).

The energy density (E, μWh cm^{-2}) and power density (P, μW cm^{-2}) of the supercapacitor device were obtained by the following formula:

$E = (C_S \times V^2) / (2 \times 3.6)$

$P = (3600 \times E) / \Delta t$

Supplementary figures

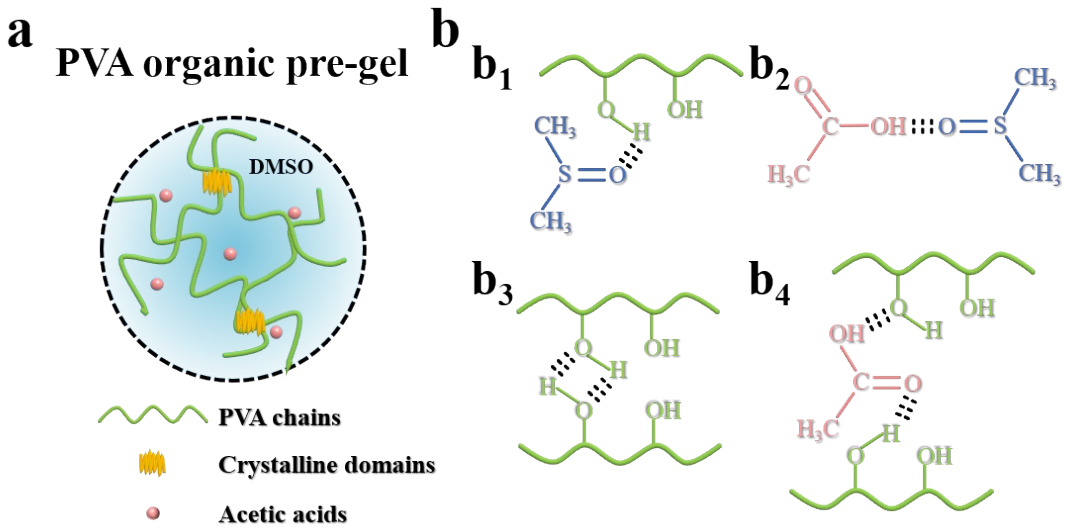

Fig. S1 (a) Structural schematic illustration of the PVA organic pre-gel. (b) Hydrogen bonds in the PVA organic pre-gel.

When acetic acid is introduced into the PVA/DMSO system. as a strong hydrogen-bond donor, the carboxylic group of acetic acid can establish strong hydrogen bonds with the O atoms on the hydrogen-bond acceptor DMSO (Fig. S1b_2), which are energetically favored over the hydrogen bonds between DMSO and hydroxyl groups on the PVA chains (Fig. S1b_1). As a consequence, the hydrogen bonding sites of the PVA are released and the intra/inter-chain hydrogen bonds of the PVA are reestablished partially (Fig. S1b_3). Meanwhile, partial acetic acids could establish potent hydrogen bonds with PVA (Fig. S1b_4), acting as a ‘‘molecular bridge’’ to enable the formation of PVA organic pre-gels. More importantly, this disruption and reconstruction of hydrogen bonds can lead to the development of crystalline domains, which can significantly contribute to the enhancement of the mechanical properties of PVA pre-gels.[7]

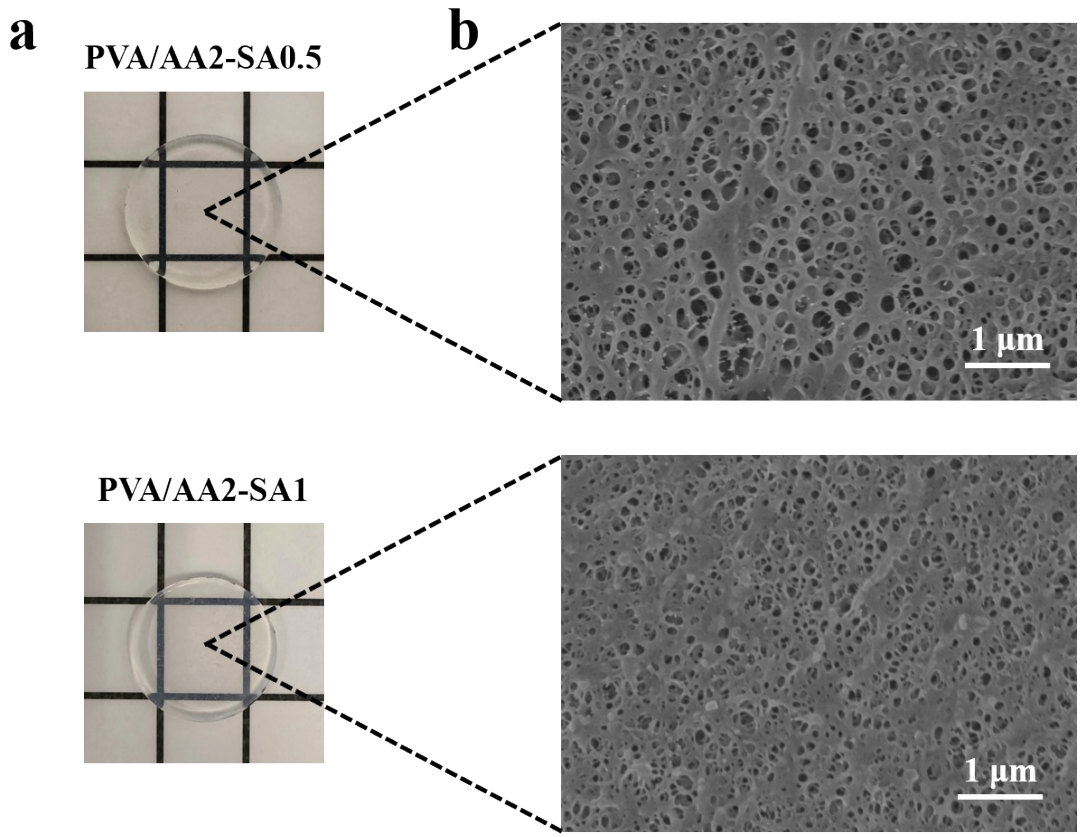

Fig. S2 (a) Digital photographs and (b) SEM images of the PVA/AA2-SA0.5 and PVA/AA2-SA1 hydrogel (all initial pre-gels are 20 mm in diameter). The background grid size in the photographs is 10 mm.

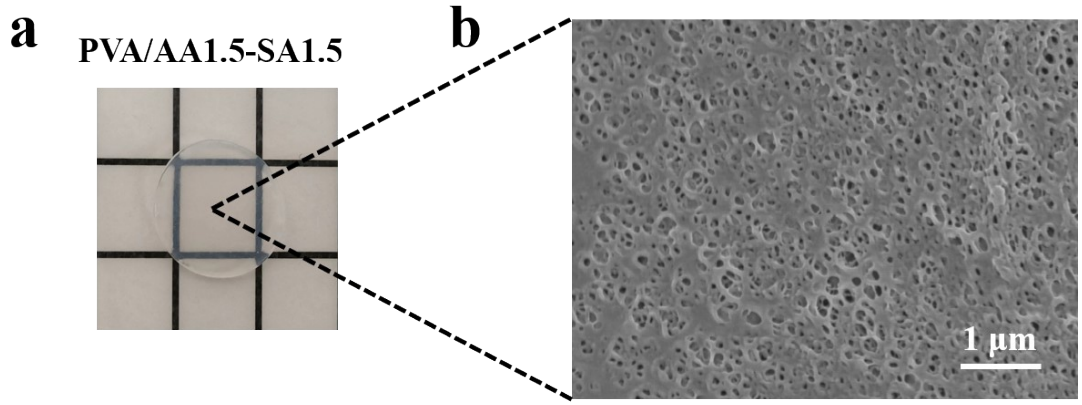

Fig. S3 (a) Digital photograph and (b) SEM image of the PVA/AA1.5-SA1.5 hydrogel (the initial PVA/AA1.5 pre-gels is 20 mm in diameter). The background grid size in the photograph is 10 mm.

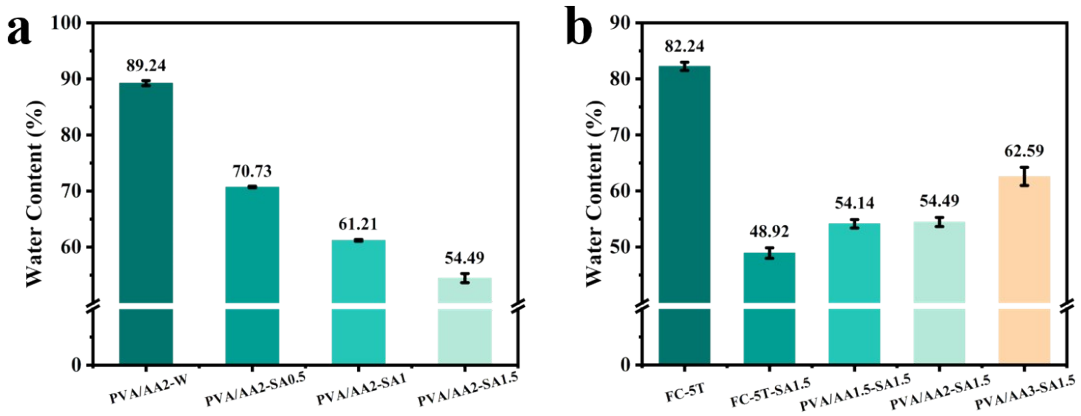

Fig. S4 The water content of (a) PVA/AA2 pre-gel after 24 h of immersion in sodium sulfate solutions with various concentrations from 0 to 1.5 M, and (b) freeze-thawed PVA hydrogel (FC-5T), FC-5T-SA1.5 hydrogel, and synergistic PVA hydrogels with different initial AA induction concentrations.

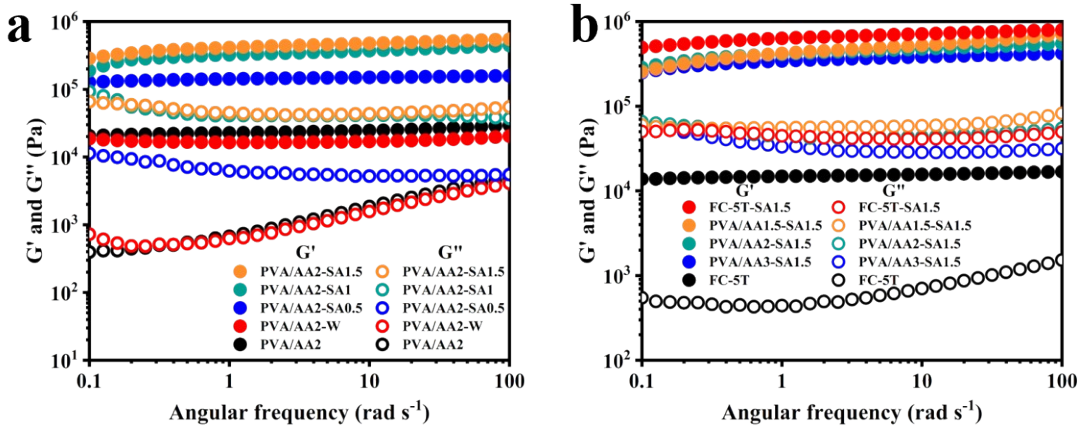

Fig. S5 G' and G" as functions of frequency for (a) initial PVA/AA2 pre-gel and after 24 h of immersion in sodium sulfate solutions with various concentrations from 0 to 1.5 M, and (b) freeze-thawed PVA hydrogel (FC-5T), freeze-thawed assisted salting-out PVA hydrogel (FC-5T-SA1.5), and synergistic PVA hydrogels with different initial AA induction concentrations.

Rheological measurements were also conducted to verify the network structural enhancement of the PVA gels caused by the synergistic effect of acetic acid induction and salting-out. As shown in Fig. S5a, the Storage modulus (G') and loss moduli (G") of the PVA/AA2-W hydrogel were lower than those of the initial PVA/AA2 pre-gel, suggesting a looser network structure and deteriorated mechanical properties that were driven by the reduction of cross-linking points due to acetic acid diffusion. Whereas the G' and G" progressively rose with increasing salt concentrations after the PVA/AA2 pre-gel was equilibrated in the salt solution, indicating the formation of denser networks. As depicted in Fig. S5b, when the PVA pre-gels induced by different AA concentrations equilibrated in the salt solution of the same concentration (1.5 M), the G' and G" exhibited different

levels, with the G' and G'' decreasing as the initial induced AA concentration increased, which is well in line with the volume retraction and pore reduction trend, revealing a progressively looser network. In the meantime, we tested the G' and G" of the freeze-thawed PVA hydrogel (FC-5T) and corresponding PVA hydrogel following 1.5 M Na_2SO_4 solution immersion (FC-5T-SA1.5). As anticipated, after salting solution soaking, the G' and G" of FC-5T-SA1.5 hydrogel significantly outperformed the FC-5T. It should be mentioned that FC-5T-SA1.5 hydrogel expressed a higher G' but lower G" value in comparison to PVA/AA1.5-SA1.5 hydrogel, implying that it had a denser network but lagged behind in terms of network uniformity.

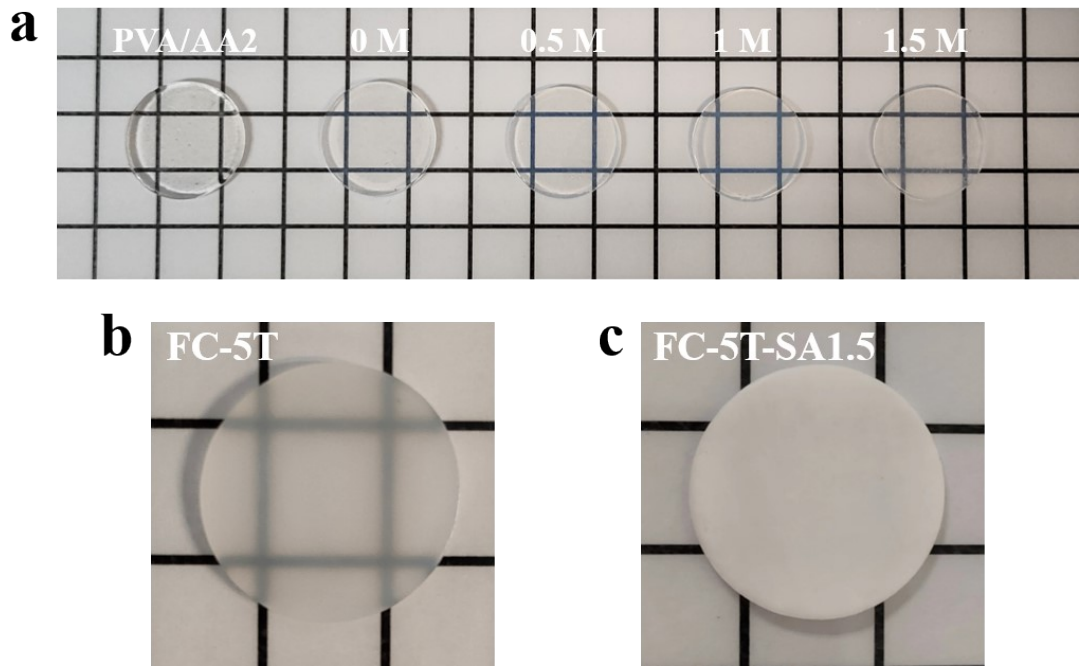

Fig. S6 Digital photographs of (a) initial PVA/AA2 pre-gel and after 24 h of immersion in sodium sulfate solutions with various concentrations from 0 to 1.5 M, (b) freeze-thawed hydrogel (FC-5T), and (c) freeze-thawed assisted salting-out hydrogel (FC-5T-SA1.5). The background grid size in the photographs is 10 mm.

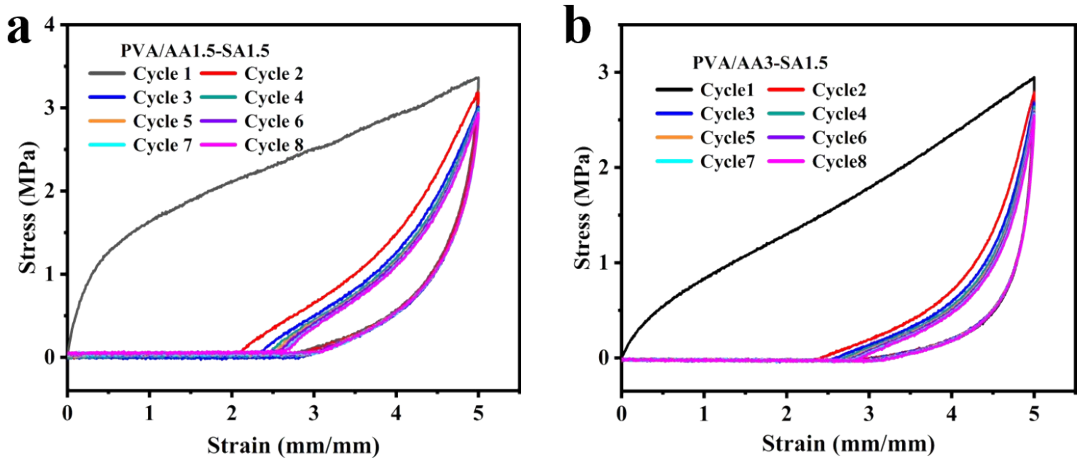

Fig. S7 Successive loading-unloading curves of (g) PVA/AA1.5-SA1.5 and (h) PVA/AA3-SA1.5 hydrogel with eight cycles under a fixed strain (λ = 5).

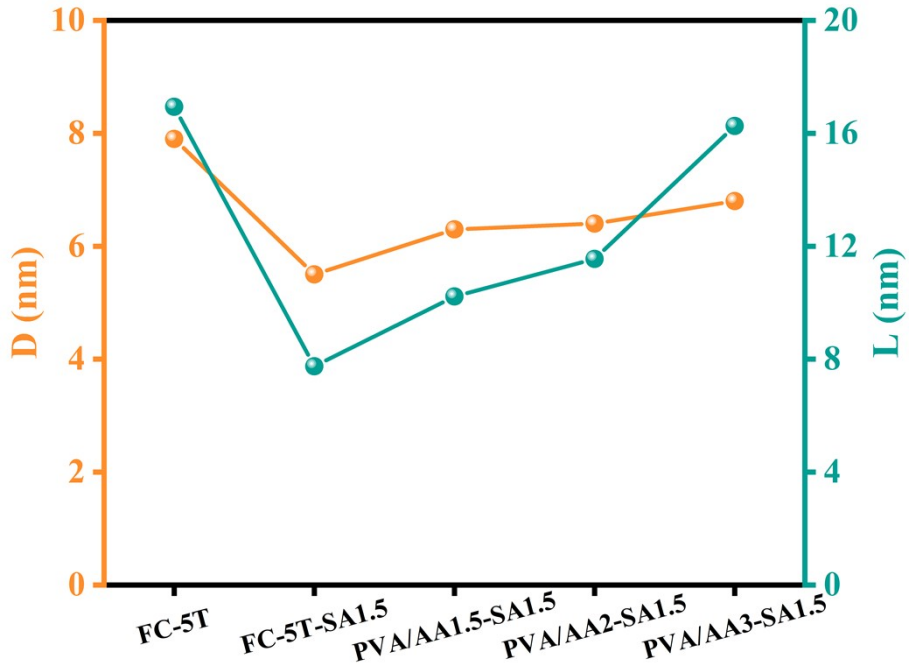

Fig. S8 The average size of crystalline domains (D) and the average distance between adjacent crystalline domains (L) of the freeze-thawed PVA hydrogel (FC-5T), freeze-thawed assisted salting-out PVA hydrogel (FC-5T-SA1.5), and synergistic PVA hydrogel with different initial AA concentrations.

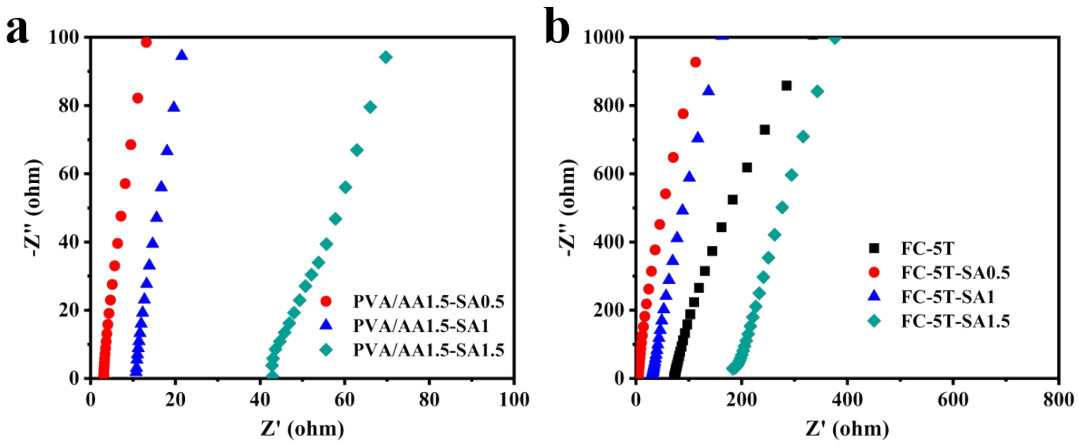

Fig. S9 EIS curves of (a) PVA/AA1.5 pre-gel and (b) FT-5C hydrogel after 24 h of immersion in sodium sulfate solutions with various concentrations.

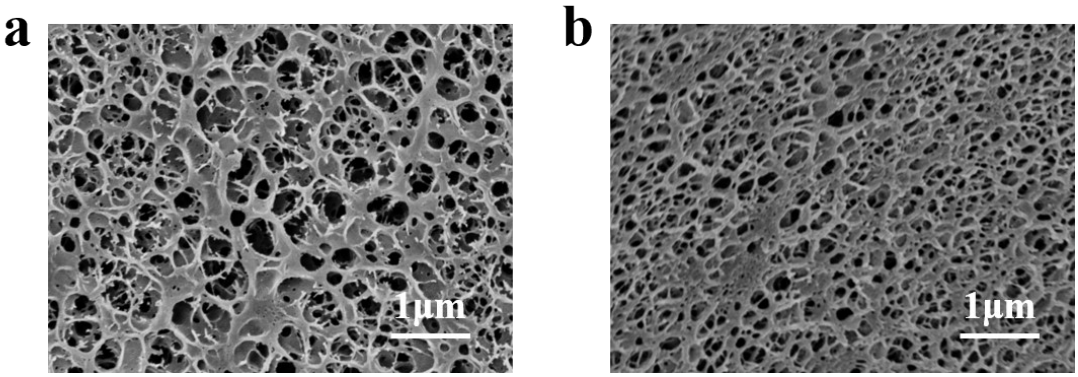

Fig. S10 SEM images of (a) PVA/AA3-SA0.5 hydrogel, and (b) PVA/AA3-SA1 hydrogel.

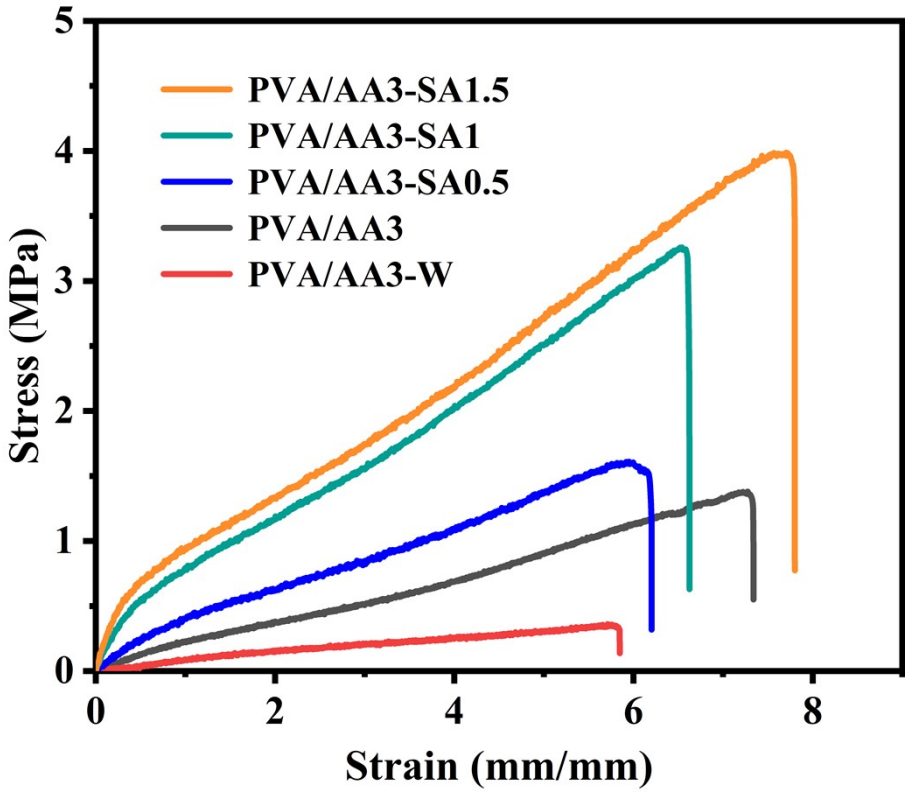

Fig. S11 Representative tensile stress-strain curves of initial PVA/AA3 pre-gel and after 24 h of immersion in sodium sulfate solutions with various concentrations from 0 to 1.5 M.

Fig. S11 illustrates the stress-strain curves of a series of hydrogels obtained by soaking the PVA/AA3 pre-gels in different concentrations of Na_2SO_4 solutions. After soaking the PVA/AA3 pre-gels in Na_2SO_4 solution, the gels can achieve a significant increase in the mechanical characteristics, and continuously enhance with the increment of the concentration. The "PVA/AA3-SA1" hydrogel can achieve a strength of 3.26 MPa and an elongation of 662%, showing a significant improvement over the previous hydrogel electrolyte.

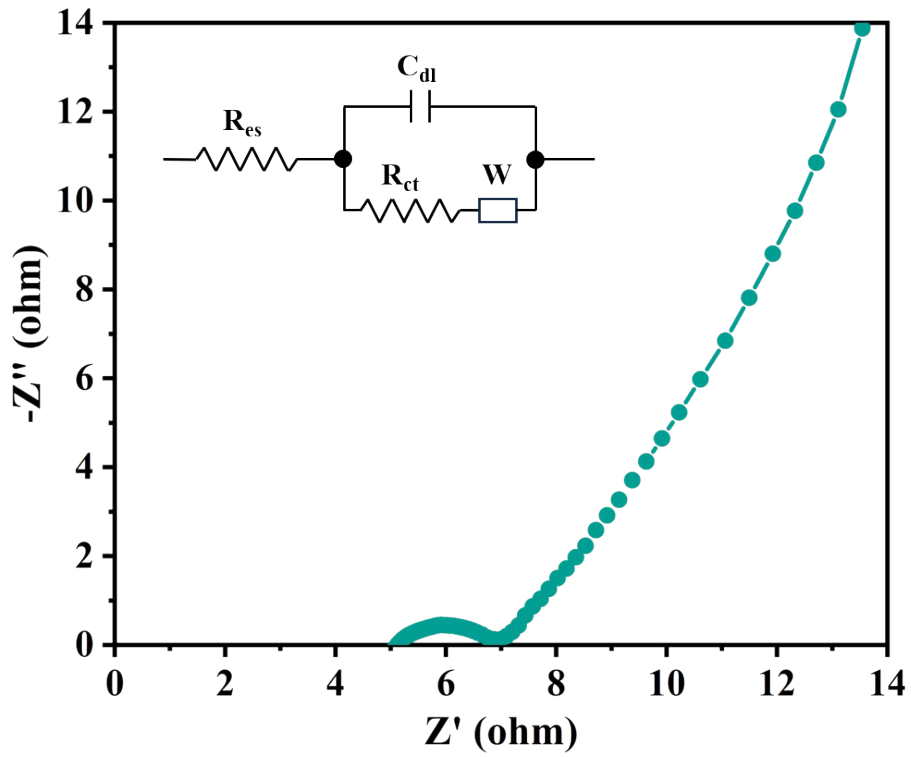

Fig. S12 Nyquist plot of the assembled supercapacitor.

The impedance characteristics of the assembled supercapacitor is illustrated in Fig. S12. After simplifying the series-parallel circuit, Z-view software was used to establish the equivalent circuit model and for fitting the EIS spectra. The intercept of the curves at the high frequency of the real axis represents the equivalent series resistance (R_{es}), including the ionic resistance of the electrolyte, the intrinsic resistance of the electrode, and their contact resistance. The semicircle in the middle-high frequency corresponds to the charge-transfer resistance (R_{ct}) and its relative double-layer capacitance (C_{dl}). The straight line at low frequency denotes the Warburg impedance (W). According to the equivalent current diagram, the R_{es} of the supercapacitor is 5.13 Ω, demonstrating its small intrinsic resistance, and the R_{ct} value of the supercapacitor is 3.05 Ω, indicating that it has good charge transfer kinetics.

Table. S1 Comparison of supercapacitor prepared in this work with previously reported supercapacitors with conducting polymer electrodes and hydrogel electrolytes.

electrolyte	mechanical property	electrode	capacitance	reference
PVA/PAMAA/H_2SO_4	0.44 MPa, 608%	PANI	95.8 mF cm^{-2} at 0.2 mA cm^{-2}	5
PVA/H_2SO_4	0.47 MPa, 380%	SWCNF/PANI	15.8 mF cm^{-2} at 0.044 mA cm^{-2}	8
PVA/PA	0.32 MPa, 800%	PANI/PA/PVA	22.8 mF cm^{-2} at 0.2 mA cm^{-2}	9
PAAm/Alg/$AlCl_3$	N/A, 500%	PPy/CNT	52.3 mF cm^{-2} at 2 mA cm^{-2}	10
PAA/H_3PO_4	0.16 MPa, 900%	PPy/CNT	0.1 mF cm^{-2} at 1.7 μA cm^{-2}	11
P(NaSS)/P(VBIm-Cl)/PVA	N/A	PANI/nw-$WO_{2.72}$/AuNPs	61 mF cm^{-2} at 0.1 mA cm^{-2}	12
PAm/VSNPs	0.3 MPa, 1500%	PPy/CNT	41.6 mF cm^{-2} at 1 mA cm^{-2}	13
PVA/Na_2SO_4	3.26 MPa, 662%	PANI/CC	73.1 mF cm^{-2} at 0.5 mA cm^{-2}	This work

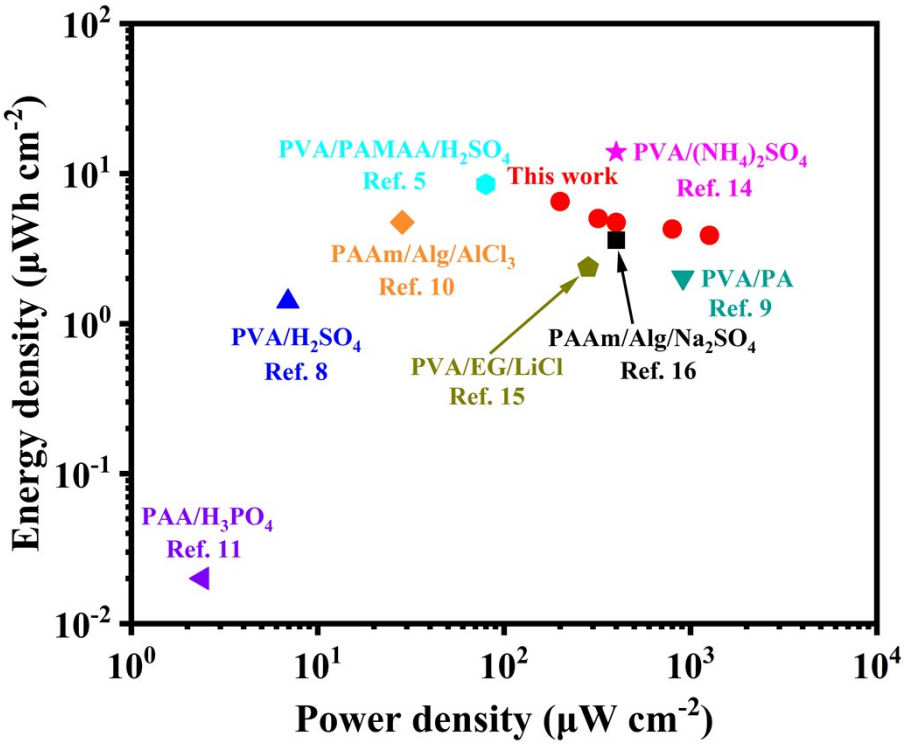

Fig. S13 Ragone plots of the assembled supercapacitor in this work compared with previously reported flexible hydrogel-based supercapacitors: PVA/PAMAA/H_2SO_4[5], PVA/H_2SO_4[8], PVA/PA[9], PAAm/Alg/$AlCl_3$[10], PVA/H_3PO_4[11], PVA/$(NH_4)_2SO_4$[14], PVA/EG/LiCl[15], PAAm/Alg/Na_2SO_4[16].

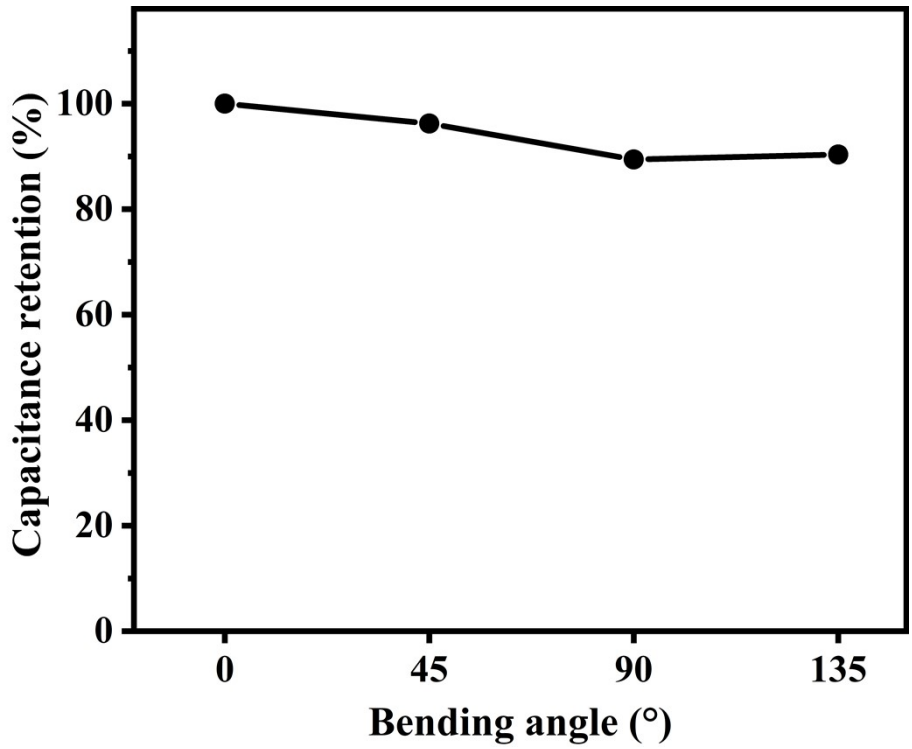

Fig. S14 Capacitance retention of the assembled supercapacitor at 1.0 mA cm^{-2} under different bending angles.

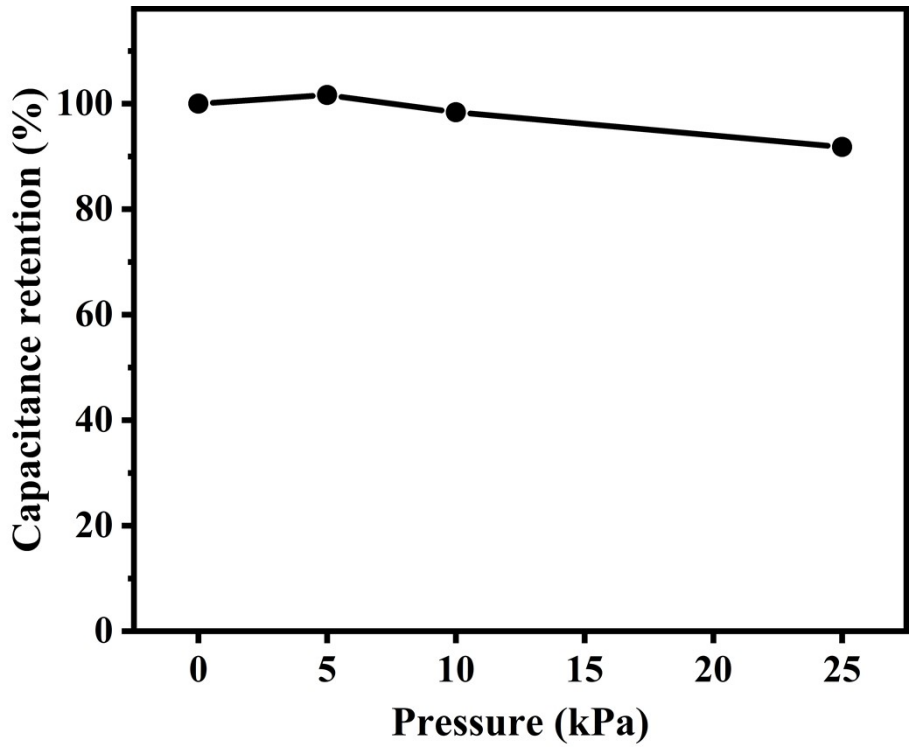

Fig. S15 Capacitance retention of the assembled supercapacitor at 1.0 mA cm^{-2} under different pressures.

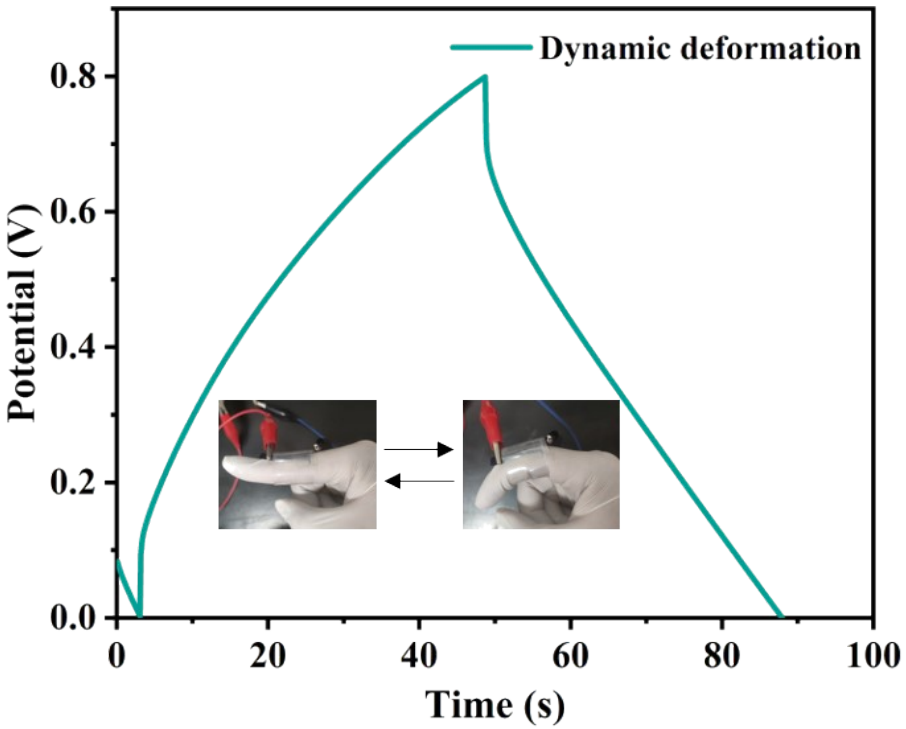

Fig. S16 GCD curves of the assembled supercapacitors under dynamic deformation.

To demonstrate the potential of our prepared hydrogel for wearable devices, we tested the charge-discharge characteristics of the assembled supercapacitor by taping it to the index finger and dynamically deforming it between the extended and bent states. As shown in the Fig. S16, the supercapacitor is capable of maintaining good and stable energy output under continuous dynamic deformation, which illustrates its significant potential for flexible wearable applications.

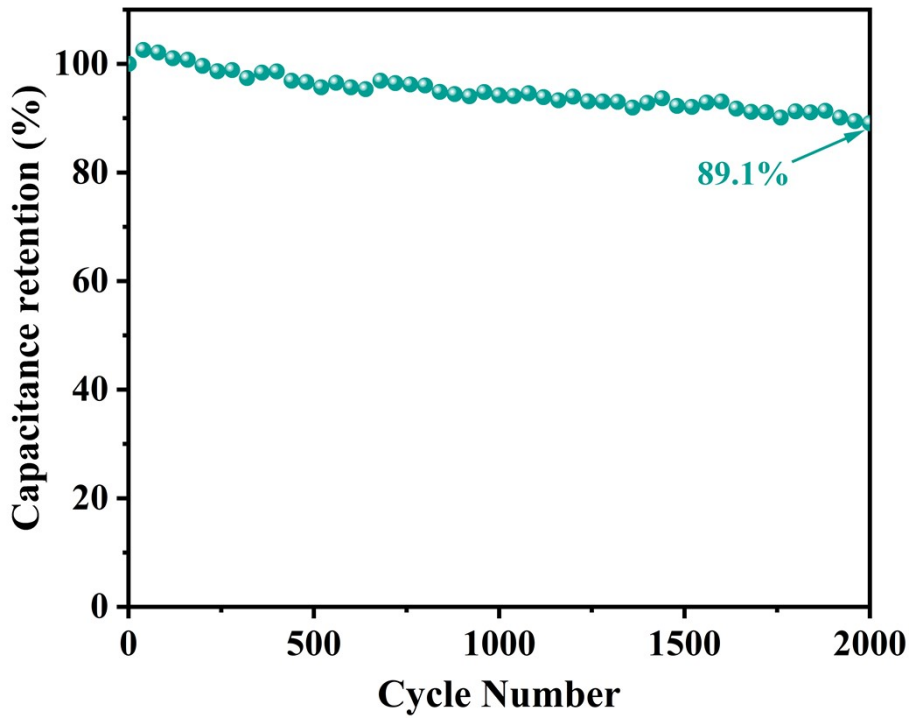

Fig. S17 Capacitance retention of the assembled supercapacitor at 1 mA cm^{-2} after 2000 charging and discharging process

As shown in Fig. S17, the areal specific capacitance of the assembled supercapacitor was maintained at 89.1% of the initial areal specific capacitance after 2000 cycles of galvanostatic charge-discharge at 1 mA cm^{-2}, illustrating its good stability under prolonged successive operation.

Reference

1 S. Lin, J. Liu, X. Liu and X. Zhao, Proc Natl Acad Sci U S A, 2019, 116, 10244-10249.
2 N. A. Peppas and E. W. Merrill, Journal of Applied Polymer Science, 1976, 20, 1457-1465.
3 S. T. Lin, X. Y. Liu, J. Liu, H. Yuk, H. C. Loh, G. A. Parada, C. Settens, J. Song, A. Masic, G. H. McKinley and X. H. Zhao, Sci Adv, 2019, 5, eaau8528.
4 A. L. Patterson, Physical Review, 1939, 56, 978-982.
5 J. Huang, S. Han, J. Zhu, Q. Wu, H. Chen, A. Chen, J. Zhang, B. Huang, X. Yang and L. Guan, Advanced Functional Materials, 2022, 32, 2205708.
6 T. Cheng, F. Wang, Y.-Z. Zhang, L. Li, S.-Y. Gao, X.-L. Yang, S. Wang, P.-F. Chen and W.-Y. Lai, Chemical Engineering Journal, 2022, 450, 138311.
7 W. Zhong, Y. Song, S. Yang, L. Gong, D. Shi, W. Dong and H. Zhang, Soft Matter, 2023, 19, 355-360.
8 Y. Guo, K. Zheng and P. Wan, Small, 2018, 14, 1704497.
9 Y. Wang, C. Lv, G. Ji, R. Hu and J. Zheng, Journal of Materials Chemistry A, 2020, 8, 8255-8261.
10 Z. Liu, G. Liang, Y. Zhan, H. Li, Z. Wang, L. Ma, Y. Wang, X. Niu and C. Zhi, Nano Energy, 2019, 58, 732-742.
11 M. Hu, J. Wang, J. Liu, J. Zhang, X. Ma and Y. Huang, Chemical Communications, 2018, 54,

6200-6203.
12 G. Li, L. Gao, L. Li and L. Guo, J. Alloys Compd., 2019, 786, 40-49.
13 Y. Huang, M. Zhong, F. Shi, X. Liu, Z. Tang, Y. Wang, Y. Huang, H. Hou, X. Xie and C. Zhi, Angew. Chem. Int. Ed. 2017, 56, 9141-9145.
14 J. Chen, D. Shi, Z. Yang, W. Dong and M. Chen, Journal of Power Sources, 2022, 532, 231326.
15 Q. Rong, W. Lei, J. Huang and M. Liu, Advanced Energy Materials, 2018, 8, 1801967.
16 J. Zeng, L. Dong, W. Sha, L. Wei and X. Guo, Chemical Engineering Journal, 2020, 383, 123098.